Energy & Environmental Science

ROYAL SOCIETY OF CHEMISTRY

PAPER

View Article Online
View Journal

Cite this: DOI: 10.1039/d2ee01421a

Breaking the sodium solubility limit for extraordinary thermoelectric performance in p-type PbTe†

Yingcai Zhu, [a] Lei Hu, [b] Shaoping Zhan,[a] Toshiaki Ina,[c] Xiang Gao,[d] Tao Hong*[a] and Li-Dong Zhao *[ae]

Received 3rd May 2022,
Accepted 28th July 2022

DOI: 10.1039/d2ee01421a

rsc.li/ees

The thermoelectric performance of a given material is closely related to its carrier concentration. However, the maximum solubility of dopants in matrixes is a key limitation for improving the carrier concentration, which may result in an underestimated figure-of-merit *ZT*. Here we show that Na solubility in the PbTe–*x*% $AgInSe_2$ (LISST) system is largely enhanced exceeding its conventional solubility limit. The enhanced Na solubility facilitates band convergence corroborated by the Pisarenko relationship and temperature-dependent Hall coefficient measurements. Accordingly, we achieve a large power factor of ~28.4 μW cm^{-1} K^{-2} at 873 K for $Pb_{0.95}Na_{0.05}Te$–0.5% $AgInSe_2$. In addition, the lattice thermal conductivity is suppressed with increasing Na content. Hence, the quality factor is largely boosted especially at high temperatures due to the enhanced weighted mobility and depressed lattice thermal conductivity. Consequently, an ultrahigh figure-of-merit *ZT* of ~2.5 at 773 K and a large average *ZT* (ZT_{avg}) of ~1.5 at 323–873 K are achieved in $Pb_{0.95}Na_{0.05}Te$–0.5% $AgInSe_2$. Our findings demonstrate that a synergistic optimization of electrical and thermal properties can be realized through breaking the solubility limit of the doped component, providing a promising path for the enhancement of thermoelectric performance.

Broader context

The compromise between the Seebeck coefficient and electrical conductivity indicates that an optimum carrier concentration is indispensable for good thermoelectric performance. However, the solubility of dopants in matrixes is a limiting factor for manipulating the carrier concentration of materials. Experimentally, the solubility limit is often judged by observation of the impurity phase, which will often underestimate the maximum dopant solubility. The maximum solubility of dopants could be achieved in the multiphase region. In this work, we found that sodium solubility is largely enhanced with the introduction of $AgInSe_2$ in $Pb_{1-y}Na_yTe$ matrixes. Local structure analysis using X-ray absorption fine structure (XAFS) spectra demonstrates that it is prone to form an $AgInTe_2$ secondary phase and Se_{Te} defects in this system. These will suppress the formation of Te vacancies (V_{Te}), which is the origin of the enhanced sodium solubility and doping efficiency. Moreover, the improved sodium solubility facilitates band convergence. A combination of enhanced power factor and reduction of lattice thermal conductivity results in an ultrahigh figure-of-merit *ZT* of ~2.5 at 773K for the $Pb_{0.95}Na_{0.05}Te$–0.5% $AgInSe_2$ sample. Our findings reveal that breaking the solubility limit of dopants is a promising way to improve the thermoelectric performance.

[a] *School of Materials Science and Engineering, Beihang University, Beijing, 100191, China. E-mail: hongtao77@buaa.edu.cn, zhaolidong@buaa.edu.cn*
[b] *State Key Laboratory for Mechanical Behavior of Materials, Xi'an Jiaotong University, Xi'an, 710049, China*
[c] *Research and Utilization Division, Japan Synchrotron Radiation Research Institute (JASRI/SPring-8), Sayo, Hyogo, Japan*
[d] *Center for High Pressure Science and Technology Advanced Research (HPSTAR), Beijing, 100094, China*
[e] *Key Laboratory of Intelligent Sensing Materials and Chip Integration Technology of Zhejiang Province (2021E10022), Hangzhou Innovation Institute of Beihang University, Hangzhou, 310051, China*

† Electronic supplementary information (ESI) available: Details of experiments and calculations; XRD patterns and lattice constants (a) for $Pb_{1-y}Na_yTe$–*x*%$AgInSe_2$ (Fig. S1 and S2); XANES spectra of Te K-edge and Pb L_3-edge for $Pb_{0.98}Na_{0.02}Te$–0.5%$AgInSe_2$ (Fig. S3); the calculated Se K-edge XANES spectra as a function of cluster size (Fig. S4); Pisarenko plot and Hall carrier mobility for $Pb_{0.98}Na_{0.02}Te$–*x*%$AgInSe_2$ (Fig. S5); temperature-dependent Lorenz number and electrical thermal conductivity of $Pb_{0.98}Na_{0.02}Te$–*x*%$AgInSe_2$ (Fig. S6); temperature-dependent Hall carrier concentration and Hall carrier mobility for $Pb_{1-y}Na_yTe$–0.5%$AgInSe_2$ (Fig. S7); temperature-dependent Lorenz number and electrical thermal conductivity of $Pb_{1-y}Na_yTe$–0.5%$AgInSe_2$ (Fig. S8); the ADF and ABF images and EDS mappings for $Pb_{0.95}Na_{0.05}Te$–0.5%$AgInSe_2$ (Fig. S9); the reproducibility of thermoelectric properties for $Pb_{0.95}Na_{0.05}Te$–0.5%$AgInSe_2$ (Fig. S10); the figure-of-merit *ZT* as a function of reduced Fermi level at 773K and 873 K for $Pb_{1-y}Na_yTe$–0.5%$AgInSe_2$ (Fig. S11); the coordination environment around Se assuming that Se occupies the Te site in PbTe matrix (Table S1). See DOI: https://doi.org/10.1039/d2ee01421a

Introduction

The consumption of fossil fuels results in a large amount of carbon dioxide (CO_2) emission, causing serious environmental deterioration and global climate change. Thermoelectric generators can boost the energy efficiency through converting waste heat to electricity, which is an effective way to alleviate environmental problems and energy crisis. An large figure-of-merit ZT is required to achieve high conversion efficiency (η) of a thermoelectric device: $\eta = \frac{T_h - T_c}{T_h} \frac{\sqrt{1 + Z\frac{T_h - T_c}{2}} - 1}{\sqrt{1 + Z\frac{T_h + T_c}{2}} + \frac{T_c}{T_h}}$, where T_h and T_c are the hot side temperature and cold side temperature of the device, respectively. Here, Z is a function of transport parameters of materials, $Z = S^2\sigma/\kappa_{tot}$, where S is the Seebeck coefficient, σ is the electrical conductivity and κ_{tot} is the total thermal conductivity. The interdependency between these parameters is a big challenge to achieve a large Z value. To date, continuous exploration has been made to lower the thermal conductivity,[1–8] enhance the power factor (PF = $S^2\sigma$),[9–17] or seek new promising materials with ultralow lattice thermal conductivity.[18–26]

Alloying or introducing materials with low lattice thermal conductivity in matrixes is expected to enhance phonon scattering attributing to the appearance of point defects,[27] nanodots,[28] precipitates,[29] dislocations,[30] displacement layers[31] or hierarchical structures.[32] However, most nanostructures can also boost carrier scattering and thus lower the electrical conductivity. Additionally, the carrier concentration can be largely affected due to the incorporation of defects. Both Seebeck coefficient and electrical conductivity are functions of the carrier concentration and the compromise between these parameters requires an optimum carrier concentration to achieve a maximum power factor. Therefore, further carrier engineering is often required.[33] For example, adding extra Ag in $Ag_nPb_{100}In_nTe_{100+2n}$ (LIST)[29] and extra Cu in $Cu_mPb_{100}Sb_mTe_{100}Se_{2m}$ (CLAST)[32] are essential to further improve their electrical performance.

The type of carrier and the carrier concentration are determined by the dominant defects in a system. However, the solubility of dopants is a limiting factor to achieve a large carrier concentration. Moreover, the solubility of dopants was often underestimated and the solubility limit is expected to be achieved in the multiphase region.[34] Accordingly, the strategy of phase boundary mapping was employed to investigate the dopant solubility and develop advanced thermoelectric materials.[35–37] Improving the solubility of dopants is desirable to modulate the carrier concentration and thus enhance the thermoelectric performance of materials.

Lead chalcogenides (PbQ, Q = Te, Se, and S) have received great scientific attention due to their promising thermoelectric performance.[38–47] In particular, PbTe exhibits the best thermoelectric properties among these lead chalcogenides, which have been used as a component of thermoelectric generators in the early NASA space missions. The superior thermoelectric properties of PbTe benefit from the band convergence,[12,48,49] resonant levels,[50,51] strong phonon anharmonicity[52] and all-scale hierarchical architectures.[2,53] A maximum ZT value larger than 2 was achieved in recent works.[2,54] In practical applications, the average figure-of-merit ZT (ZT_{avg}) is more important to realize large conversion efficiency for a thermoelectric generator. However, only limited works have achieved a ZT_{avg} of $\sim$1.5 in PbTe-based materials.[55,56]

In this work, ternary $AgInSe_2$ with low thermal conductivity[57–59] is introduced into the $Pb_{0.98}Na_{0.02}Te$ matrix first, achieving a maximum ZT of $\sim$2.0 at 773 K. The room temperature ZT is largely enhanced to $\sim$0.5 with increasing $AgInSe_2$ content attributing to the depressed thermal conductivity and decreased carrier concentration. Then, we manipulated the carrier concentration of $Pb_{1-y}Na_yTe$–0.5% $AgInSe_2$ by changing the Na content. Interestingly, the carrier concentration of $Pb_{1-y}Na_yTe$–0.5% $AgInSe_2$ increases with increasing Na content (y, y = 0.01–0.06) without observing saturation, which is much higher than that of single Na-doped PbTe when $y > 0.04$ (Fig. 1a). This indicates that Na solubility is largely enhanced with the incorporation of $AgInSe_2$. Local structure and microstructure analyses were performed using X-ray absorption fine structure (XAFS) spectroscopy and scanning transmission electron microscopy (STEM) techniques to understand the mechanism of enhanced Na solubility. The improved Na solubility facilitates the band convergence between the light valence band (L) and secondary valence band (Σ) in PbTe. Therefore, $Pb_{1-y}Na_yTe$–0.5% $AgInSe_2$ (y = 0.05, 0.06) compounds possess the highest effective mass and carrier concentration compared with previous p-type PbTe-based materials[12,37,48,49,54,56,60–62] (Fig. 1b). The bipolar effect is also suppressed with Na-doping, leading to an ultralow thermal conductivity. As a result, the quality factor is largely enhanced. Finally, a maximum ZT of $\sim$ 2.5 at 773 K and an average ZT of $\sim$ 1.5 at 323–873 K are obtained in p-type $Pb_{0.95}Na_{0.05}Te$–0.5% $AgInSe_2$ (Fig. 1c and d).

Results and discussion

Crystal structure and lattice occupation of dopants

X-ray diffraction (XRD) measurements were performed for $Pb_{1-y}Na_yTe$–x% $AgInSe_2$ samples (Fig. S1, ESI†). There is no impurity phase observed in the XRD patterns. The lattice constant (a) of $Pb_{0.98}Na_{0.02}Te$–x% $AgInSe_2$ decreases with increasing $AgInSe_2$ content (Fig. S2a, ESI†). The lattice constant (a) of $Pb_{1-y}Na_yTe$ increases slightly when $y > 0.02$ (Fig. S2b, ESI†) due to the limitation of sodium solubilty in the PbTe matrix. Interestingly, the lattice constant (a) of $Pb_{1-y}Na_yTe$–0.5% $AgInSe_2$ shows a continuous decrease tendency with increasing Na-doping content (Fig. S2b, ESI†), revealing the enhanced sodium solubility.

X-ray absorption fine structure spectra were recorded to investigate the crystal structure and the atomic occupation of doping elements for $Pb_{0.98}Na_{0.02}Te$–0.5% $AgInSe_2$. Compared with the X-ray absorption near-edge structure (XANES) of Te K-edge of PbTe, there is almost no change for the XANES of Te K-edge of $Pb_{0.98}Na_{0.02}Te$–0.5% $AgInSe_2$ (Fig. S3a, ESI†). A similar phenomenon was also observed in the comparison of XANES of Pb L_3-edge between PbTe and $Pb_{0.98}Na_{0.02}Te$–0.5%

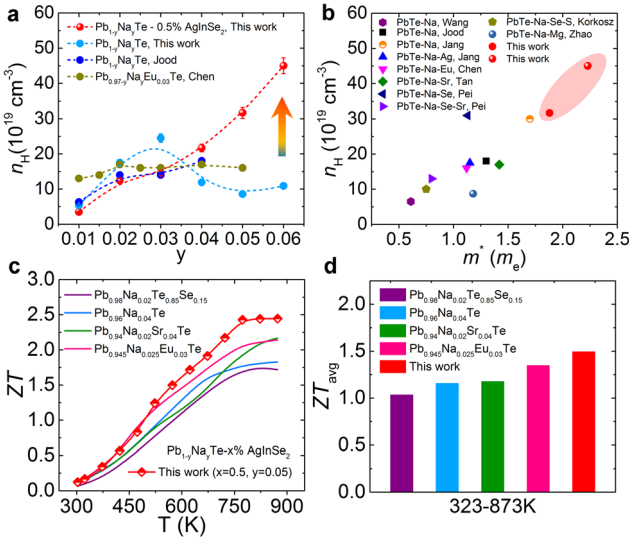

Fig. 1 (a) Carrier concentration as a function of Na content (y) for Na-doped PbTe-based materials. (b) Carrier concentration as a function of effective mass for p-type PbTe-based materials. Comparison of (c) ZT values and (d) average ZT at 323–873 K for various PbTe-based compounds.

$AgInSe_2$ (Fig. S3b, ESI†). These results indicate that the introduction of $AgInSe_2$ and Na in PbTe did not alter its NaCl-type cubic crystal structure, which is consistent with the XRD results.

The four main features (A, B, C, and D) in the XANES of Ag K-edge of $Pb_{0.98}Na_{0.02}Te$–0.5% $AgInSe_2$ well correspond with the XANES features (1, 2, 3, and 4) of Ag K-edge of $AgInTe_2$ (Fig. 2a), whereas they have lots of difference compared with

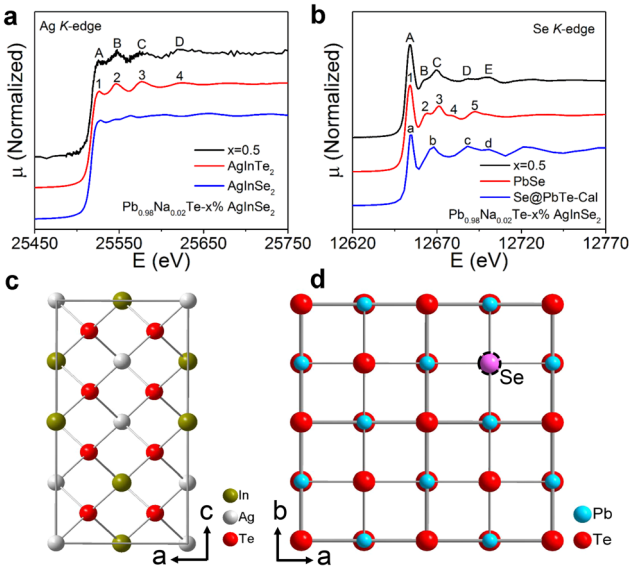

Fig. 2 (a) Experimental XANES spectra at Ag K-edge for $Pb_{0.98}Na_{0.02}Te$–0.5% $AgInSe_2$ (black line), $AgInTe_2$ (red line), and $AgInSe_2$ (blue line). (b) Experimental XANES spectra at Se K-edge for $Pb_{0.98}Na_{0.02}Te$–0.5% $AgInSe_2$ (black line), PbSe (red line). The blue line represents the calculation of the Se K-edge XANES spectrum assuming that the Se atoms occupy Te sites in the PbTe matrix. (c and d) Crystal structure of $AgInTe_2$ and PbTe.

the XANES of Ag K-edge of $AgInSe_2$. Therefore, most of the Ag or In atoms form the $AgInTe_2$ secondary phase (Fig. 2c) in the LISST system. Accordingly, the occupation site of the Se atom in the LISST system is analyzed. In Fig. 2b, the A, B, and C peaks in the XANES of Se K-edge of $Pb_{0.98}Na_{0.02}Te$–0.5% $AgInSe_2$ are well reflected in the XANES of Se K-edge of PbSe.However, we cannot find similar features corresponding to the D and E features in the XANES of Se K-edge of PbSe. Then, we calculated the XANES of Se K-edge assuming that Se replaces the Te site in the PbTe matrix. Interestingly, the D and E features are well consistent with the features (c and d) in our calculated XANES spectrum of Se-doped PbTe. These two features (c and d) are mainly derived from the multiple scattering of photoelectrons by the nearest-three shells around Se (Fig. S4 and Table S1, ESI†). The calculated Se K-edge XANES spectra as a function of cluster size (R) also reveal that these calculations are almost converged when $R > 6.5$ Å (Fig. S4, ESI†). We can conclude that a part of Se atoms occupy the Te sites in PbTe matrixes (Fig. 2d). The local structure analysis demonstrates a complex atomic coordination environment in the LISST system and this will have a significant effect on the defect impurities and the electrical and thermal transport properties in the LISST system.

Thermoelectric properties of $Pb_{0.98}Na_{0.02}Te$–x% $AgInSe_2$

The electrical conductivity of $Pb_{0.98}Na_{0.02}Te$–x% $AgInSe_2$ decreases with elevated temperatures (Fig. 3a), indicating a degenerate semiconductor behavior. Additionally, the electrical conductivity is largely depressed with the increasing content of $AgInSe_2$. Typically, the values decrease from $\sim$2940 S cm^{-1} to $\sim$300 S cm^{-1} at room temperature. Room-temperature Hall measurements reveal that the carrier concentrations are reduced from 1.75 $\times$ 10^{20} cm^{-3} to 1.1 $\times$ 10^{19} cm^{-3} with the introduction of $AgInSe_2$ (Fig. S5a, ESI†), which is the main reason for the decrease of electrical conductivity. In particular, the low-temperature ($T < 373$ K) electrical conductivities for several samples are reduced more significantly, which may be attributed to grain boundary scattering.[63] Similarly, the experimental Hall carrier mobility of $Pb_{0.98}Na_{0.02}Te$–x% $AgInSe_2$ is smaller than the theoretical value estimated by the single parabolic band (SPB) model and it also shows a non-monotonic changing behavior with the increasing $AgInSe_2$ content (Fig. S5b, ESI†), which should be attributed to the combined effect of grain boundary scattering and downtrend of carrier concentration.

The positive Seebeck coefficients shown in Fig. 3b reveal a p-type semiconductor behavior. The Seebeck coefficient is largely enhanced over the whole temperature range with the incorporation of $AgInSe_2$. The pisarenko relationship for $Pb_{0.98}Na_{0.02}Te$–x% $AgInSe_2$ indicates that their effective masses have no significant change with varying $AgInSe_2$ contents (Fig. S5a, ESI†). Therefore, the enhancement of Seebeck coefficient is mainly due to the reduction of carrier concentration. The temperature-dependent Seebeck coefficient of $Pb_{0.98}Na_{0.02}Te$ shows a continuous increasing tendency and no peak is observed, demonstrating that there is no obvious bipolar effect. However, an apparent saturation behavior of Seebeck coefficient

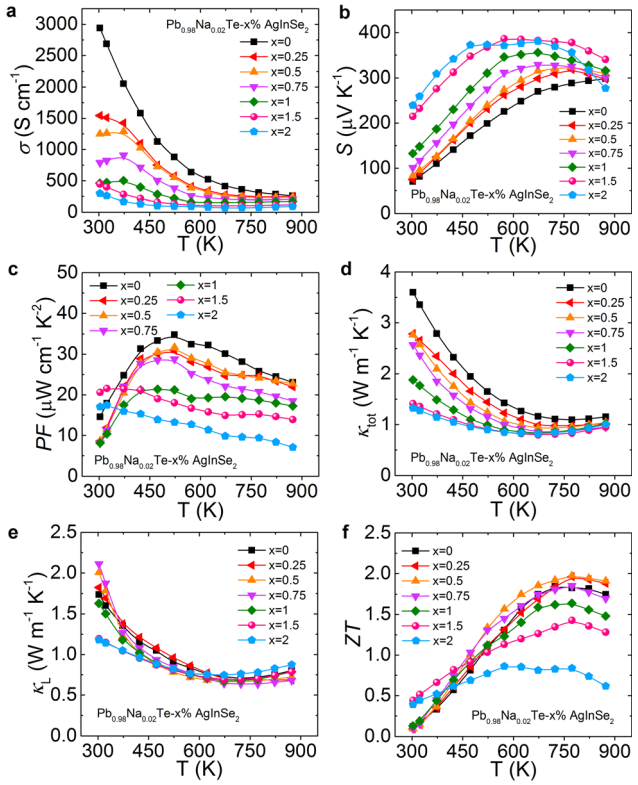

Fig. 3 Temperature-dependent (a) electrical conductivity, (b) Seebeck coefficient, (c) power factor, (d) total thermal conductivity, (e) lattice thermal conductivity and (f) figure-of-merit ZT for $Pb_{0.98}Na_{0.02}Te$–x% $AgInSe_2$.

can be observed with increasing temperatures when $x > 0.75$. The bipolar effect is mainly attributed to the suppressed carrier concentration. Hence,the power factor decreases with the incorporation of $AgInSe_2$ over the entire temperature range when $x < 1$ (Fig. 3c). Interestingly, the room-temperature power factor is enhanced from $\sim$14.5 μW cm^{-1} K^{-2} to $\sim$20.6 μW cm^{-1} K^{-2} for $Pb_{0.98}Na_{0.02}Te$–1.5% $AgInSe_2$ due to the boosted Seebeck coefficient.

The total thermal conductivity (κ_{tot}) of $Pb_{0.98}Na_{0.02}Te$–x% $AgInSe_2$ compounds is shown in Fig. 3d. Apparently, the κ_{tot} decreases with the increasing $AgInSe_2$ content. The room-temperature κ_{tot} of $Pb_{0.98}Na_{0.02}Te$ is $\sim$3.6 W m^{-1} K^{-1}, which decreases to $\sim$1.32 W m^{-1} K^{-1} for the $Pb_{0.98}Na_{0.02}Te$–2% $AgInSe_2$ sample. We estimated the electrical thermal conductivity (κ_e) based on the Wiedemann–Franze law ($\kappa_e = L\sigma T$), in which the Lorenz number (L) was calculated using the single parabolic band (SPB) model assuming acoustic phonon scattering dominates (Fig. S6a, ESI†). The electrical thermal conductivity (κ_e) is largely depressed due to the reduction of electrical conductivity (Fig. S6b, ESI†). Additionally, we obtained the lattice thermal conductivity (κ_L) by subtracting κ_e from κ_{tot}, which also shows a downturn with the introduction of $AgInSe_2$ (Fig. 3e). Since obvious grain boundary scattering is observed in the low temperature region ($T < 373$ K), the estimation of Lorenz number may be insufficient and thus lead to an overestimated lattice thermal conductivity at this temperature range. The upturn of lattice thermal conductivity at high temperatures for the $Pb_{0.98}Na_{0.02}Te$–2% $AgInSe_2$ sample arises from the bipolar effect. Benefitting from the reduction of total thermal conductivity, we achieved a high figure-of-merit ZT of $\sim$2.0 at 773 K for $Pb_{0.98}Na_{0.02}Te$–0.5% $AgInSe_2$ (Fig. 3f). In addition, a synergistic effect of enhanced power factor and suppressed thermal conductivity results in a good ZT of $\sim$0.5 at room temperature for $Pb_{0.98}Na_{0.02}Te$–1.5% $AgInSe_2$.

Enhanced sodium solubility and band convergence in $Pb_{1-y}Na_yTe$–0.5% $AgInSe_2$

Given that the carrier concentration is largely decreased with the incorporation of $AgInSe_2$ in the LISST system, we further modulated the Na content to optimize the thermoeletric properties in the current optimal composition ($Pb_{0.98}Na_{0.02}Te$–0.5% $AgInSe_2$). The temperature-dependent electrical conductivity of $Pb_{1-y}Na_yTe$–0.5% $AgInSe_2$ is shown in Fig. 4a. With Na content increasing, the electrical conductivity shows an inverse trend compared with the introduction of $AgInSe_2$ in the LISST system and its value is largely boosted. Similarly, grain boundary scattering is also observed for several samples in the low temperature range. Room-temperature Hall measurements show that the carrier concentration is largely enhanced from $\sim 3.5 \times 10^{19}$ cm^{-3} to $\sim 4.5 \times 10^{20}$ cm^{-3} with increasing Na content (Fig. 4b), which explains the enhancement of electrical conductivity. Accordingly, the Hall carrier mobility is decreased from $\sim$212 cm^2 V^{-1} s^{-1} to $\sim$32 cm^2 V^{-1} s^{-1} (Fig. 4b). The Seebeck coefficients slightly decrease with Na doping and their temperature-dependent values show a continuous increasing trend and no saturation peaks are observed when $y > 0.03$ (Fig. 4c), indicating a suppressed bipolar effect. As a result, the power factor is enhanced and a maximum value of $\sim$ 37.4 μW cm^{-1} K^{-2} at 523 K and a high power factor of $\sim$ 28.4 μW cm^{-1} K^{-2} at 873 K are achieved for the $Pb_{0.95}Na_{0.05}Te$–0.5% $AgInSe_2$ compound (Fig. 4d).

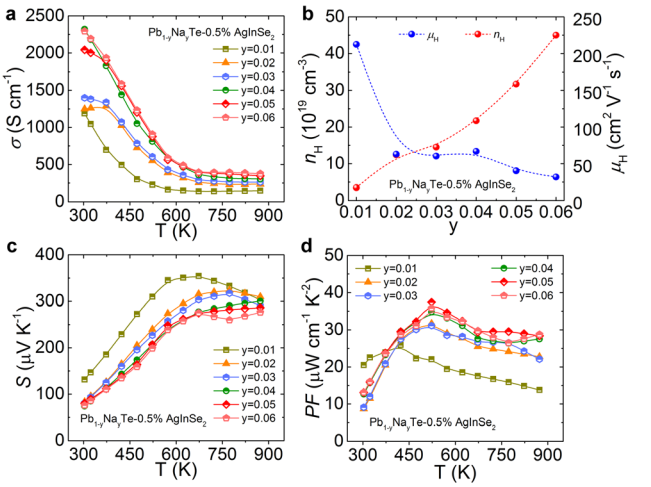

Fig. 4 (a) Temperature-dependent electrical conductivity of $Pb_{1-y}Na_yTe$–0.5% $AgInSe_2$. (b) The room-temperature Hall carrier concentration (n_H) and carrier mobility (μ_H) with increasing sodium content (y). Temperature-dependent (c) Seebeck coefficient and (d) power factor for $Pb_{1-y}Na_yTe$–0.5% $AgInSe_2$.

The optimization of carrier concentration plays a key factor in the enhancement of power factor. The significant increase of carrier concentration shown in Fig. 4b is surprising and let us reconsider the solubility of Na dopants in PbTe. A previous study showed that the solubility limit of Na in PbTe was very small (~0.5%)[64] and a larger Na solubility may be obtained at high temperatures (~1.4%).[65] Recent work has shown enhanced Na solubility (>2%) in PbTe but with poor doping efficiency that the carrier concentration has no obvious improvement.[37] The room-temperature carrier concentration of $Pb_{0.96}Na_{0.04}Te$ is only $\sim 1.8 \times 10^{20}$ cm^{-3}.[37] In sharp contrast, a much higher carrier concentration of $\sim 4.5 \times 10^{20}$ cm^{-3} can be achieved for $Pb_{0.94}Na_{0.06}Te$–0.5% $AgInSe_2$, revealing a boosted Na solubility. Assuming each Na atom donates one hole, the carrier concentration of $\sim 4.5 \times 10^{20}$ cm^{-3} corresponds to $y = 0.03$ in $Pb_{1-y}Na_yTe$ at 100% doping efficiency. The perfect doping efficiency is hard to achieve due to the formation of intrinsic defects in real systems. Additionally, the introduction of $AgInSe_2$ will largely suppress the carrier concentration in LISST systems (Fig. S5a, ESI†). Therefore, the actual Na solubility in $Pb_{0.94}Na_{0.06}Te$–0.5% $AgInSe_2$ will be much higher than 3%.

In the ternary Pb–Te–Na phase diagram (Fig. 5a), the PbTe–Na_2Te line corresponds to a composition of $Pb_{1-y}Na_yTe_{1-y/2}$ and the formation of Te vacancies will compensate all holes introduced by Na doping, which represents the "valence balanced" line. The PbTe–NaTe line reflects a stoichiometry of $Pb_{1-y}Na_yTe$ with 100% doping efficiency. In Fig. 5b, the phase boundary of PbTe follows the PbTe–NaTe line initially when the Na content is small, whereas it approaches the "valence balanced" line with the increasing Na content (blue region) due to the limited Na solubility and the existence of killer defects (such as V_{Te}, Te_{Pb}). Consequently, the Na doping efficiency is weakened. Intriguingly, the large carrier concentration of $Pb_{0.94}Na_{0.06}Te$–0.5% $AgInSe_2$ indicates enhanced Na solubility and doping efficiency, which can be reflected by the extension of the phase boundary (red region) in the phase diagram (Fig. 5b). It was reported that the Na_2Te compound possesses the lowest formation energy in the Pb–Te–Na phase diagram.[66] Additionally, the intrinsic defects (V_{Te} and Te_{Pb}) in PbTe have low formation energy.[66,67] These mark the origin of the low Na solubility and doping efficiency in PbTe. With the introduction of $AgInSe_2$ into the PbTe matrix, it is prone to form a secondary phase of $AgInTe_2$ and Se_{Te} defects demonstrated by our local structure analysis (Fig. 2), which can suppress the formation of Te vacancies and Te anti-site defects. A similar phenomenon was also observed in a previous study.[61] Due to V_{Te} defect annihilation, the Na solubility and doping efficiency are largely enhanced in the LISST system.

The enhanced sodium solubility is also demonstrated and confirmed by microstructure analysis using the aberration-corrected scanning transmission electron microscopy (STEM) techniques. Fig. 6a and d show the annular bright-field (ABF) STEM images for the $Pb_{0.95}Na_{0.05}Te$ and $Pb_{0.95}Na_{0.05}Te$–0.5% $AgInSe_2$ samples, respectively, at the same magnification. Obviously, the morphology comparison between these two samples reveals that the $Pb_{0.95}Na_{0.05}Te$–0.5% $AgInSe_2$ sample has a higher defect density. The ABF images of these two

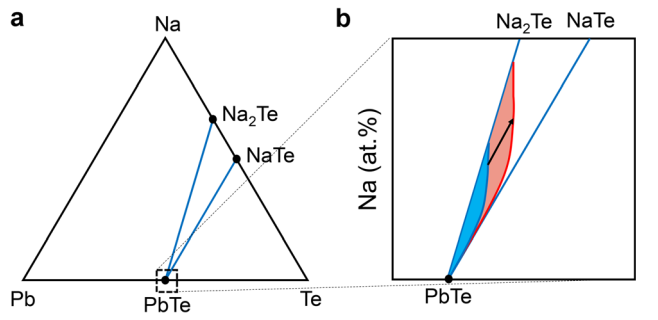

Fig. 5 (a) Ternary phase diagram of Pb–Te–Na. (b) Schematic diagram of the enlarged region close to the PbTe phase. The phase boundary extends from the blue region to the red region revealing the enhancement of Na solubility and doping efficiency.

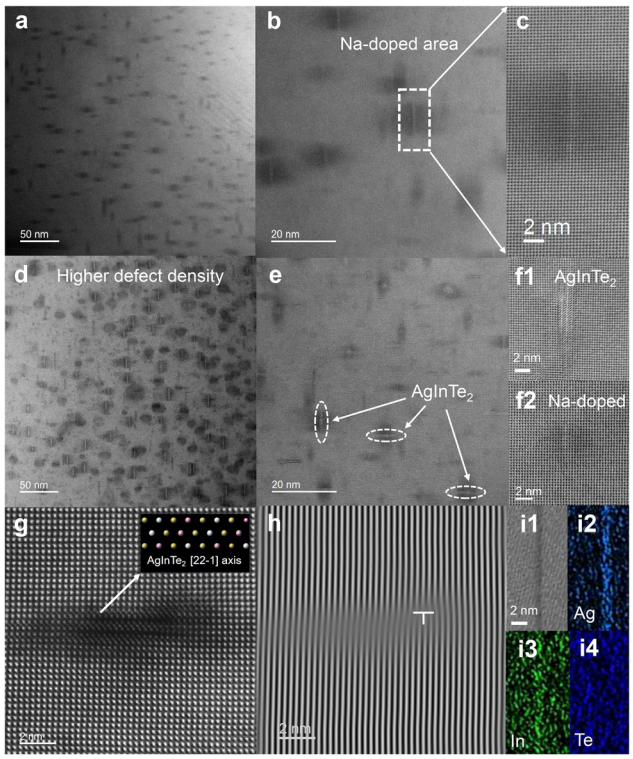

Fig. 6 Microstructure observation in $Pb_{0.95}Na_{0.05}Te$ and $Pb_{0.95}Na_{0.05}Te$–0.5% $AgInSe_2$, respectively. (a and b) The STEM-ABF images of the $Pb_{0.95}Na_{0.05}Te$ sample at different magnifications in the [100] axis, and (d and e) show the same magnification ABF images as (a and b) of the $Pb_{0.95}Na_{0.05}Te$–0.5% $AgInSe_2$ sample in the same [100] direction. (c) The substitution of Na for Pb sites causes the defect contrast in (b). (f1) The atomic-scale $AgInTe_2$ precipitates (circled by a dashed line in (e)) and (f2) the occupation of Na on Pb sites induce two obvious contrasts in (e). (g) The HAADF image shows the atomic-scale $AgInTe_2$ precipitates in the PbTe matrix, and the inset represents the atomic structure of $AgInTe_2$ from the [22−1] axis. (h) The inverse fast Fourier transform image of (g) indicates the formation of dislocations in the matrix due to the presence of the $AgInTe_2$. (i1-4) ADF image and the EDS mappings of the atomic-scale $AgInTe_2$ precipitates.

samples at the same high magnification are shown in Fig. 6b and e. There is only one type of defect contrast in the $Pb_{0.95}Na_{0.05}Te$ sample (Fig. 6b), resulting from the substitution of Na for Pb sites, which does not change the lattice arrangement of PbTe, but only the contrast in intensity (Fig. 6c). By contrast, two obvious contrasts are included in the $Pb_{0.95}Na_{0.05}Te$–0.5% $AgInSe_2$ sample (Fig. 6e). One is caused by the atomic-scale $AgInTe_2$ precipitates (Fig. 6f1) and the other is still induced by Na occupying Pb sites (Fig. 6f2). Clearly, a significant increase of the Na doping sites can be observed in the $Pb_{0.95}Na_{0.05}Te$–0.5% $AgInSe_2$ sample (Fig. 6d and e), indicating the enhanced sodium solubility.

The Pisarenko relationship was plotted to understand the enhancement of power factor. As shown in Fig. 7a, the Seebeck coefficients almost remain unchanged with increasing carrier concentration when $y > 0.02$ and this tendency is largely deviated from the theoretical line (black line) estimated using the SPB model. Accordingly, the effective mass (m^*) of the LISST system is largely enhanced from $\sim$0.8 m_e to $\sim$2.2 m_e with increasing Na content at room temperature (Fig. 7b), which is even larger than the effective mass ($\sim$1.42 m_e) of $Pb_{0.98}Na_{0.02}$-Te–6%SrTe.[56] These phenomena indicate a complex electronic band structure behavior in the LISST system. Various works have already proved that Na-doping can decrease the band offset between the light valence band (L) and the secondary valence band (Σ) in PbQ and lead to band convergence.[37,68] Moreover, we show that the solubility of Na doping is largely enhanced, which will facilitate band convergence in the LISST system. Therefore, a two-band model was developed to understand the anomalous deviation tendency. The calculation details can be found in the ESI.† Intriguingly, the experimental results can be well reflected by the two-band model (red line in Fig. 7a) considering the contribution of both the valence band (L) and secondary valence band (Σ). The band convergence tendency is also verified by our temperature-dependent Hall measurements. The temperature-dependent Hall coefficients (R_H) for several samples show a peak at $\sim$423 K (Fig. 6c), indicating a redistribution of carrier and band convergence behavior.[40,48] The effective masses (m^*) as a function of temperature were estimated using the SPB model (Fig. 7d). Typically, the effective mass increases from $\sim$1.3 m_e to $\sim$7.0 m_e with increased temperatures for the $y = 0.04$ sample. The largely enhanced effective mass is also consistent with the band convergence behavior. Consequently, the band convergence behavior enables the enhancement of power factor in the LISST system. The temperature-dependent Hall carrier concentrations increase with the increasing Na content in the whole temperature range (Fig. S7a, ESI†), revealing the enhanced Na solubility in the LISST system. There is a flat region for the Hall carrier mobilty (μ_H) when $T < 423$K (Fig. S7b, ESI†), which is retained due to the grain boundary scattering. Then, the Hall carrier mobilities follow a μ_H–T^{-4} relationship when $T > 423$K (Fig. S7b, ESI†). Generally, a μ_H–$T^{-1.5}$ relationship indicates that the acoustic-phonon scattering dominates. Here, the deviation from this relationship is mainly attributed to the enhanced effective masses with increasing temperatures.

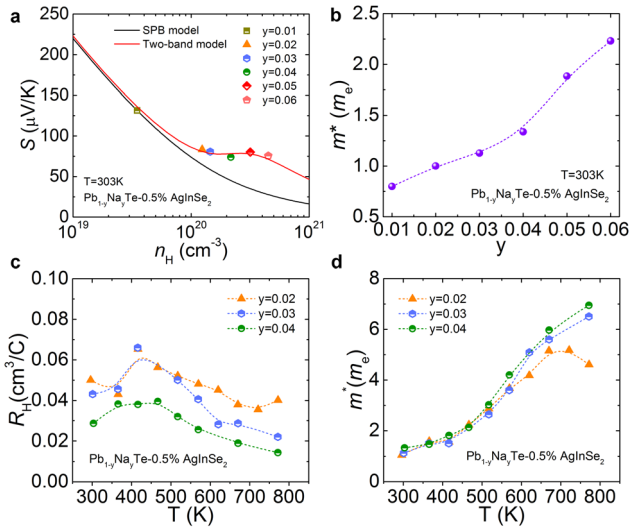

Fig. 7 (a) Pisarenko plot for $Pb_{1-y}Na_yTe$–0.5% $AgInSe_2$ at room temperature. The dots represent the experimental results, the black line was calculated using the SPB model while the red line was simulated using a two-band model. (b) Room-temperature effective masses (m^*) of $Pb_{1-y}Na_yTe$–0.5% $AgInSe_2$ calculated using the SPB model. (c) Hall coefficients (R_H) and (d) effective masses as a function of temperature for $Pb_{1-y}Na_yTe$–0.5% $AgInSe_2$.

Thermal transport properties and the figure-of-merit *ZT* of $Pb_{1-y}Na_yTe$–0.5% $AgInSe_2$

The total thermal conductivity (κ_{tot}) of $Pb_{1-y}Na_yTe$–0.5% $AgInSe_2$ is enhanced with increased Na-doping (Fig. 8a), which is mainly attributed to the improvement of electrical thermal conductivity (κ_e, Fig. S8, ESI†). Given that obvious grain boundary scattering exists at the low temperature region, the estimation of Lorenz number (L) using the SPB model may be insufficient (Fig. S8, ESI†). Therefore, the lattice thermal conductivity (κ_{lat}) follows an irregular change tendency with Na doping at low temperatures (Fig. 8b). The flat temperature-dependent lattice thermal conductivity of $Pb_{1-y}Na_yTe$–0.5% $AgInSe_2$ (y = 0.05, 0.06) from about 450–600 K may due to the Na diffusion at high temperatures. A similar phenomenon was observed in the PbTe-SrTe-Na system.[2] However, in the most interesting high temperature range ($T > 600$ K), the κ_{lat} values are largely suppressed with Na doping. Typically, the κ_{lat} value decreases from $\sim$0.79 W m^{-1} K^{-1} to $\sim$0.47 W m^{-1} K^{-1} at 773 K. There is no obvious upturn tendency for κ_{lat} with increasing temperatures when $y > 0.01$, revealing a negligible bipolar contribution to the total thermal conductivity, which can be attributed to the bandgap opening with Na doping.[37,54] Additionally, previous works already proved that Na-doping will introduce point defects, nano-precipitates, and grain boundaries into the PbQ matrixes, scattering heat-carrying phonons with different mean free paths.[2,64] Here, we already observed a higher defect density in the $Pb_{0.95}Na_{0.05}Te$–0.5% $AgInSe_2$ sample compared with the $Pb_{0.95}Na_{0.05}Te$ sample (Fig. 6a, b, d and e). The spindle-shaped $AgInTe_2$ precipitates with a dozen nanometers and spherical nanostructures with tens of nanometers were observed in

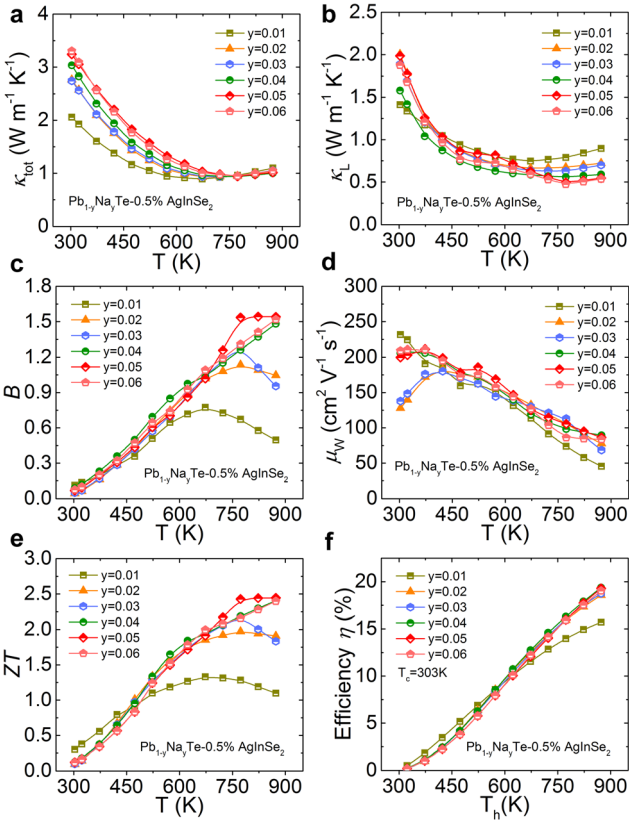

Fig. 8 Temperature-dependent (a) total thermal conductivity, (b) lattice thermal conductivity (c) quality factor B, (d) weighted mobility, and (e) the figure-of-merit ZT for $Pb_{1-y}Na_yTe$–0.5% $AgInSe_2$. (f) Theoretical power generation efficiency as a function of hot-side temperature (T_h) for $Pb_{1-y}Na_yTe$–0.5% $AgInSe_2$. The cold-side temperature (T_c) is set at 303 K.

$Pb_{0.95}Na_{0.05}Te$–0.5% $AgInSe_2$ (Fig. 6e and Fig. S9, ESI†). Additionally, the high angle annular dark filed (HAADF) image for the $Pb_{0.95}Na_{0.05}Te$–0.5% $AgInSe_2$ sample reveals atomic-scale $AgInTe_2$ precipitates (Fig. 6g), which causes the formation of dislocations in the PbTe matrix (Fig. 6h). The morphology and composition of these precipitates were displayed in an annular dark field (ADF) image and the corresponding energy dispersive X-ray spectroscopy (EDS) mappings (Fig. 6i). These hierarchical architectures observed in LISST will cause strong phonon scattering. Therefore, a combination effect of suppression of bipolar effects and strong phonon scattering leads to the reduction of lattice thermal conductivity in the LISST system.

The dimensionless quality factor (B) is a good indicator of the thermoelectric performance for a given material. The following equations[69,70] were used to calculate the quality factor B:

$$B = \left(\frac{k_B}{e}\right)^2 \frac{\sigma_{E_0} T}{\kappa_L} \quad (1)$$

$$\sigma_{E_0} = \frac{\sigma}{F_0(\eta)} = \frac{8\pi e(2m_e k_B T)^{3/2}}{3h^3}\mu_W \quad (2)$$

Here, k_B is the Boltzmann constant, e is the electron charge, σ_{E_0} is the transport coefficient, $F_0(\eta)$ is the Fermi-Dirac integral, h is the Planck constant, and μ_w represents the weighted mobility. Fig. 8c shows that the quality factor continuously increases with increasing temperatures when the Na-doping content $y > 0.03$. The quality factor is largely enhanced with Na-doping especially at high temperatures and a maximum value of ~1.54 at 773 K is obtained for $Pb_{0.95}Na_{0.05}Te$–0.5% $AgInSe_2$. The eqn (1) and (2) indicate that the B value is proportional to the μ_w/κ_L. A large reduction of lattice thermal conductivity was already observed at high temperatures with Na-doping. The depressed weighted mobility at low temperatures mainly arises from the appearance of grain boundary scattering (Fig. 8d). Interestingly, the weighted mobility is enhanced at high temperatures with Na-doping (Fig. 8d), which is mainly due to the band convergence tendency. Therefore, the large Na solubility and doping efficiency enable a combined effect of boosted weighted mobility and suppressed lattice thermal conductivity at high temperatures. As a result, the optimization of quality factor B reveals an enhancement of thermoelectric properties. Large ZT values of >2.4 at 873 K can be obtained for several samples (y = 0.04–0.06), as shown in Fig. 8e. In particular, the ZT values approach to 2.5 when $T >$ 773 K for $Pb_{0.95}Na_{0.05}Te$–0.5% $AgInSe_2$. Moreover, the thermoelectric properties of $Pb_{0.95}Na_{0.05}Te$–0.5% $AgInSe_2$ show good repeatability and the ZT value is reproducible considering its uncertainty (Fig. S10, ESI†). The ZT value as a function of reduced Fermi level (η) indicates that the ZT is almost optimized (Fig S11, ESI†). A large theoretical power generation efficiency of ~19% was achieved (Fig. 8f), indicating promising practical applications.

Conclusions

In summary, we achieved a large ZT of ~2.0 at 773 K and a good ZT of ~0.5 at room temperature by introduction of $AgInSe_2$ into the $Pb_{0.98}Na_{0.02}Te$ matrix. By further optimizing the carrier concentration with Na-doping, a maximum ZT of ~2.5 at 773 K and an average ZT of ~1.5 at 323–873 K were obtained for $Pb_{0.95}Na_{0.05}Te$–0.5% $AgInSe_2$. The solubility of Na was largely enhanced, which facilitated both band convergence and further reduction of lattice thermal conductivity. Consequently, the weighted mobility and the quality factor B were largely improved. The enhanced Na solubility may be due to the suppression of Te vacancies or Te anti-site defects as the formation of $AgInTe_2$ secondary phase and Se_{Te} defects revealed by our local structure analysis using X-ray absorption fine structure spectra. This work demonstrates that the Na solubility limit and doping efficiency were underestimated, and $Pb_{0.95}Na_{0.05}Te$ and $Pb_{0.94}Na_{0.06}Te$ are promising initial matrixes for further optimization. Our findings indicate that maximizing the solubility of dopants is a promising way to improve the thermoelectric performance. It will be more interesting and practical to use low-cost and rich elements for tuning the solubility of dopants.

Experimental section

High-purity raw materials, Pb (99.999%), Te (99.999%), Na (99.9%), Ag (99.99%), In (99.99%), and Se (99.999%) were

weighed in a stoichiometric ratio ($Pb_{1-y}Na_yTe$–x% $AgInSe_2$) and flame sealed in carbon coating silica tubes. The silica tubes were loaded in a muffle furnace and heated to 1423 K for 24 h and then soaked at this temperature for 10 h and subsequently the furnace was cooled down to room temperature. The obtained ingots were hand-ground to powders and then sintered at 873 K for 6 minutes (SPS-211Lx) under a pressure of 50 MPa. We obtained highly dense bulk samples (>97% of theoretical density). The Seebeck coefficient and electrical conductivity were measured under a He atmosphere using a ULVAC RIKO ZEM-3 instrument. We measured the thermal diffusivity (D) using a laser flash method (Netzsch LFA-457). The heat capacity (C_p) was estimated using the Dulong-Petit law, and the density is determined by the dimensions and mass of the samples. The combined uncertainty of all measurements for determining the ZT is less than 20%. We measured the Hall coefficient (R_H) using the Van der Pauw method (Lake Shore 8400). The XRD patterns were measured using a D/MAX 2500 PC system with Cu K_α radiation. Transmission electron microscopy (TEM) was conducted using a JEOL ARM200F equipped with a cold field emission gun and an ASCOR probe corrector. The X-ray absorption fine structure (XAFS) measurements were conducted at the BL01B1 beamline of Spring-8. More details can be found in the ESI.†

Conflicts of interest

There are no conflicts to declare.

Acknowledgements

The authors thank BL01B1 at Spring-8 for the XAFS experiments (Proposal Number: 2021B1109). This work was supported by the National Natural Science Foundation of China (52002011, 52002042 and 51772012), the National Key Research and Development Program of China (2018YFA0702100 and 2018YFB0703600), the Beijing Natural Science Foundation (JQ18004), and the 111 Project (B17002). L.-D. Z. acknowledges the support from the National Science Fund for Distinguished Young Scholars (51925101).

Notes and references

1 B. Poudel, Q. Hao, Y. Ma, Y. C. Lan, A. Minnich, B. Yu, X. A. Yan, D. Z. Wang, A. Muto, D. Vashaee, X. Y. Chen, J. M. Liu, M. S. Dresselhaus, G. Chen and Z. F. Ren, *Science*, 2008, **320**, 634–638.
2 K. Biswas, J. Q. He, I. D. Blum, C. I. Wu, T. P. Hogan, D. N. Seidman, V. P. Dravid and M. G. Kanatzidis, *Nature*, 2012, **489**, 414–418.
3 L.-D. Zhao, J. He, C.-I. Wu, T. P. Hogan, X. Zhou, C. Uher, V. P. Dravid and M. G. Kanatzidis, *J. Am. Chem. Soc.*, 2012, **134**, 7902–7912.
4 W. G. Zeier, Y. Z. Pei, G. Pomrehn, T. Day, N. Heinz, C. P. Heinrich, G. J. Snyder and W. Tremel, *J. Am. Chem. Soc.*, 2013, **135**, 726–732.
5 Y. Qiu, Y. Jin, D. Wang, M. Guan, W. He, S. Peng, R. Liu, X. Gao and L.-D. Zhao, *J. Mater. Chem. A*, 2019, **7**, 26393–26401.
6 S. Roychowdhury, T. Ghosh, R. Arora, M. Samanta, L. Xie, N. K. Singh, A. Soni, J. He, U. V. Waghmare and K. Biswas, *Science*, 2021, **371**, 722–727.
7 D. Sarkar, T. Ghosh, S. Roychowdhury, R. Arora, S. Sajan, G. Sheet, U. V. Waghmare and K. Biswas, *J. Am. Chem. Soc.*, 2020, **142**, 12237–12244.
8 A. Banik, T. Ghosh, R. Arora, M. Dutta, J. Pandey, S. Acharya, A. Soni, U. V. Waghmare and K. Biswas, *Energy Environ. Sci.*, 2019, **12**, 589–595.
9 L.-D. Zhao, G. Tan, S. Hao, J. He, Y. Pei, H. Chi, H. Wang, S. Gong, H. Xu, V. P. Dravid, C. Uher, G. J. Snyder, C. Wolverton and M. G. Kanatzidis, *Science*, 2016, **351**, 141–144.
10 W. He, D. Wang, H. Wu, Y. Xiao, Y. Zhang, D. He, Y. Feng, Y.-J. Hao, J.-F. Dong, R. Chetty, L. Hao, D. Chen, J. Qin, Q. Yang, X. Li, J.-M. Song, Y. Zhu, W. Xu, C. Niu, X. Li, G. Wang, C. Liu, M. Ohta, S. J. Pennycook, J. He, J.-F. Li and L.-D. Zhao, *Science*, 2019, **365**, 1418–1424.
11 W. Liu, X. Tan, K. Yin, H. Liu, X. Tang, J. Shi, Q. Zhang and C. Uher, *Phys. Rev. Lett.*, 2012, **108**, 166601.
12 Y. Pei, X. Shi, A. LaLonde, H. Wang, L. Chen and G. J. Snyder, *Nature*, 2011, **473**, 66–69.
13 B. Qin, D. Wang, X. Liu, Y. Qin, J.-F. Dong, J. Luo, J.-W. Li, W. Liu, G. Tan, X. Tang, J.-F. Li, J. He and L.-D. Zhao, *Science*, 2021, **373**, 556–561.
14 C. Chang, M. H. Wu, D. H. He, Y. L. Pei, C. F. Wu, X. F. Wu, H. L. Yu, F. Y. Zhu, K. D. Wang, Y. Chen, L. Huang, J. F. Li, J. He and L.-D. Zhao, *Science*, 2018, **360**, 778–783.
15 Y. Jin, D. Wang, T. Hong, L. Su, H. Shi, S. Zhan, Y. Wang, S. Wang, X. Gao, Y. Qiu and L.-D. Zhao, *Adv. Energy Mater.*, 2022, **12**, 2103779.
16 D. Wu, Y. Pei, Z. Wang, H. Wu, L. Huang, L.-D. Zhao and J. He, *Adv. Funct. Mater.*, 2014, **24**, 7763–7771.
17 C. Chang, D. Wang, D. He, W. He, F. Zhu, G. Wang, J. He and L.-D. Zhao, *Adv. Energy Mater.*, 2019, **9**, 1901334.
18 G. J. Snyder and E. S. Toberer, *Nat. Mater.*, 2008, **7**, 105–114.
19 S. Mukhopadhyay, D. S. Parker, B. C. Sales, A. A. Puretzky, M. A. McGuire and L. Lindsay, *Science*, 2018, **360**, 1455–1458.
20 L. Hu, Y.-W. Fang, F. Qin, X. Cao, X. Zhao, Y. Luo, D. V. M. Repaka, W. Luo, A. Suwardi, T. Soldi, U. Aydemir, Y. Huang, Z. Liu, K. Hippalgaonkar, G. J. Snyder, J. Xu and Q. Yan, *Nat. Commun.*, 2021, **12**, 4793.
21 L.-D. Zhao, S. H. Lo, Y. Zhang, H. Sun, G. Tan, C. Uher, C. Wolverton, V. P. Dravid and M. G. Kanatzidis, *Nature*, 2014, **508**, 373–377.
22 X. Zhang, C. Chang, Y. Zhou and L.-D. Zhao, *Materials*, 2017, **10**, 198.
23 W. He, D. Wang, J.-F. Dong, Y. Qiu, L. Fu, Y. Feng, Y. Hao, G. Wang, J. Wang, C. Liu, J.-F. Li, J. He and L.-D. Zhao, *J. Mater. Chem. A*, 2018, **6**, 10048–10056.

24 Y.-L. Pei, H. Wu, J. Sui, J. Li, D. Berardan, C. Barreteau, L. Pan, N. Dragoe, W.-S. Liu, J. He and L.-D. Zhao, *Energy Environ. Sci.*, 2013, **6**, 1750.
25 X. Liu, D. Wang, H. Wu, J. Wang, Y. Zhang, G. Wang, S. J. Pennycook and L.-D. Zhao, *Adv. Funct. Mater.*, 2019, **29**, 1806558.
26 C. Chang, G. Tan, J. He, M. G. Kanatzidis and L.-D. Zhao, *Chem. Mater.*, 2018, **30**, 7355–7367.
27 Y. Zheng, T. J. Slade, L. Hu, X. Y. Tan, Y. Luo, Z. Z. Luo, J. Xu, Q. Yan and M. G. Kanatzidis, *Chem. Soc. Rev.*, 2021, **50**, 9022–9054.
28 K. F. Hsu, S. Loo, F. Guo, W. Chen, J. S. Dyck, C. Uher, T. Hogan, E. K. Polychroniadis and M. G. Kanatzidis, *Science*, 2004, **303**, 818–821.
29 Y. Xiao, H. Wu, D. Wang, C. Niu, Y. Pei, Y. Zhang, I. Spanopoulos, I. T. Witting, X. Li, S. J. Pennycook, G. J. Snyder, M. G. Kanatzidis and L.-D. Zhao, *Adv. Energy Mater.*, 2019, **9**, 1900414.
30 L. Abdellaoui, Z. Chen, Y. Yu, T. Luo, R. Hanus, T. Schwarz, R. Bueno Villoro, O. Cojocaru-Mirédin, G. J. Snyder, D. Raabe, Y. Pei, C. Scheu and S. Zhang, *Adv. Funct. Mater.*, 2021, **31**, 2101214.
31 J. He, S. N. Girard, J.-C. Zheng, L.-D. Zhao, M. G. Kanatzidis and V. P. Dravid, *Adv. Mater.*, 2012, **24**, 4440–4444.
32 S. Wang, Y. Xiao, Y. Chen, S. Peng, D. Wang, T. Hong, Z. Yang, Y. Sun, X. Gao and L.-D. Zhao, *Energy Environ. Sci.*, 2021, **14**, 451–461.
33 B. C. Qin and L.-D. Zhao, *Mater. Lab.*, 2022, **1**, 220004.
34 S. Anand, C. Wolverton and G. J. Snyder, *Chem. Mater.*, 2022, **34**, 1638–1648.
35 S. Ohno, K. Imasato, S. Anand, H. Tamaki, S. D. Kang, P. Gorai, H. K. Sato, E. S. Toberer, T. Kanno and G. J. Snyder, *Joule*, 2018, **2**, 141–154.
36 S. Ohno, U. Aydemir, M. Amsler, J. H. Pöhls, S. Chanakian, A. Zevalkink, M. A. White, S. K. Bux, C. Wolverton and G. J. Snyder, *Adv. Funct. Mater.*, 2017, **27**, 1606361.
37 P. Jood, J. P. Male, S. Anand, Y. Matsushita, Y. Takagiwa, M. G. Kanatzidis, G. J. Snyder and M. Ohta, *J. Am. Chem. Soc.*, 2020, **142**, 15464–15475.
38 Y. Xiao, D. Wang, Y. Zhang, C. Chen, S. Zhang, K. Wang, G. Wang, S. J. Pennycook, G. J. Snyder, H. Wu and L.-D. Zhao, *J. Am. Chem. Soc.*, 2020, **142**, 4051–4060.
39 Y. Qin, T. Hong, B. Qin, D. Wang, W. He, X. Gao, Y. Xiao and L.-D. Zhao, *Adv. Funct. Mater.*, 2021, **31**, 2102185.
40 G. Tan, S. Hao, S. Cai, T. P. Bailey, Z. Luo, I. Hadar, C. Uher, V. P. Dravid, C. Wolverton and M. G. Kanatzidis, *J. Am. Chem. Soc.*, 2019, **141**, 4480–4486.
41 H. Wang, Y. Pei, A. D. LaLonde and G. J. Snyder, *Adv. Mater.*, 2011, **23**, 1366–1370.
42 B. Jiang, Y. Yu, J. Cui, X. Liu, L. Xie, J. Liao, Q. Zhang, Y. Huang, S. Ning, B. Jia, B. Zhu, S. Bai, L. Chen, S. J. Pennycook and J. He, *Science*, 2021, **371**, 830–834.
43 B. Jiang, Y. Yu, H. Chen, J. Cui, X. Liu, L. Xie and J. He, *Nat. Commun.*, 2021, **12**, 3234.
44 B.-C. Qin, Y. Xiao, Y.-M. Zhou and L.-D. Zhao, *Rare Met.*, 2018, **37**, 343–350.
45 X. Qian, H. Wu, D. Wang, Y. Zhang, J. Wang, G. Wang, L. Zheng, S. J. Pennycook and L.-D. Zhao, *Energy Environ. Sci.*, 2019, **12**, 1969–1978.
46 Y. Xiao, D. Wang, B. Qin, J. Wang, G. Wang and L.-D. Zhao, *J. Am. Chem. Soc.*, 2018, **140**, 13097–13102.
47 Y. Zhu, D. Wang, T. Hong, L. Hu, T. Ina, S. Zhan, B. Qin, H. Shi, L. Su, X. Gao and L.-D. Zhao, *Nat. Commun.*, 2022, **13**, 4179.
48 L.-D. Zhao, H. J. Wu, S. Q. Hao, C. I. Wu, X. Y. Zhou, K. Biswas, J. Q. He, T. P. Hogan, C. Uher, C. Wolverton, V. P. Dravid and M. G. Kanatzidis, *Energy Environ. Sci.*, 2013, **6**, 3346.
49 Y. Pei, G. Tan, D. Feng, L. Zheng, Q. Tan, X. Xie, S. Gong, Y. Chen, J. F. Li, J. He, M. G. Kanatzidis and L.-D. Zhao, *Adv. Energy Mater.*, 2016, **7**, 1601450.
50 J. P. Heremans, V. Jovovic, E. S. Toberer, A. Saramat, K. Kurosaki, A. Charoenphakdee, S. Yamanaka and G. J. Snyder, *Science*, 2008, **321**, 554–557.
51 J. P. Heremans, B. Wiendlocha and A. M. Chamoire, *Energy Environ. Sci.*, 2012, **5**, 5510–5530.
52 O. Delaire, J. Ma, K. Marty, A. F. May, M. A. McGuire, M. H. Du, D. J. Singh, A. Podlesnyak, G. Ehlers, M. D. Lumsden and B. C. Sales, *Nat. Mater.*, 2011, **10**, 614–619.
53 L.-D. Zhao, V. P. Dravid and M. G. Kanatzidis, *Energy Environ. Sci.*, 2014, **7**, 251–268.
54 Z. Chen, Z. Jian, W. Li, Y. Chang, B. Ge, R. Hanus, J. Yang, Y. Chen, M. Huang, G. J. Snyder and Y. Pei, *Adv. Mater.*, 2017, **29**, 1606768.
55 H. J. Wu, L.-D. Zhao, F. S. Zheng, D. Wu, Y. L. Pei, X. Tong, M. G. Kanatzidis and J. Q. He, *Nat. Commun.*, 2014, **5**, 4515.
56 G. Tan, F. Shi, S. Hao, L.-D. Zhao, H. Chi, X. Zhang, C. Uher, C. Wolverton, V. P. Dravid and M. G. Kanatzidis, *Nat. Commun.*, 2016, **7**, 12167.
57 P. Qiu, Y. Qin, Q. Zhang, R. Li, J. Yang, Q. Song, Y. Tang, S. Bai, X. Shi and L. Chen, *Adv. Sci.*, 2018, **5**, 1700727.
58 Y. Zhu, Y. Liu, M. Wood, N. Z. Koocher, Y. Liu, L. Liu, T. Hu, J. M. Rondinelli, J. Hong, G. J. Snyder and W. Xu, *Chem. Mater.*, 2019, **31**, 8182–8190.
59 Y. Zhu, B. Wei, J. Liu, N. Z. Koocher, Y. Li, L. Hu, W. He, G. Deng, W. Xu, X. Wang, J. M. Rondinelli, L.-D. Zhao, G. J. Snyder and J. Hong, *Mater. Today Phys.*, 2021, **19**, 100428.
60 H. Wang, J. H. Bahk, C. Kang, J. Hwang, K. Kim, J. Kim, P. Burke, J. E. Bowers, A. C. Gossard, A. Shakouri and W. Kim, *Proc. Natl. Acad. Sci. U. S. A.*, 2014, **111**, 10949–10954.
61 H. Jang, J. H. Park, H. S. Lee, B. Ryu, S. D. Park, H. A. Ju, S. H. Yang, Y. M. Kim, W. H. Nam, H. Wang, J. Male, G. J. Snyder, M. Kim, Y. S. Jung and M. W. Oh, *Adv. Sci.*, 2021, **8**, e2100895.
62 R. J. Korkosz, T. C. Chasapis, S. H. Lo, J. W. Doak, Y. J. Kim, C. I. Wu, E. Hatzikraniotis, T. P. Hogan, D. N. Seidman, C. Wolverton, V. P. Dravid and M. G. Kanatzidis, *J. Am. Chem. Soc.*, 2014, **136**, 3225–3237.

63 J. J. Kuo, S. D. Kang, K. Imasato, H. Tamaki, S. Ohno, T. Kanno and G. J. Snyder, *Energy Environ. Sci.*, 2018, **11**, 429–434.
64 J. He, L.-D. Zhao, J. C. Zheng, J. W. Doak, H. Wu, H. Q. Wang, Y. Lee, C. Wolverton, M. G. Kanatzidis and V. P. Dravid, *J. Am. Chem. Soc.*, 2013, **135**, 4624–4627.
65 S. A. Yamini, T. Ikeda, A. Lalonde, Y. Pei, S. X. Dou and G. J. Snyder, *J. Mater. Chem. A*, 2013, **1**, 8725.
66 J. W. Doak, K. J. Michel and C. Wolverton, *J. Mater. Chem. C*, 2015, **3**, 10630–10649.
67 A. Goyal, P. Gorai, E. S. Toberer and V. Stevanović, *npj Comput. Mater.*, 2017, **3**, 42.
68 T. C. Chasapis, Y. Lee, E. Hatzikraniotis, K. M. Paraskevopoulos, H. Chi, C. Uher and M. G. Kanatzidis, *Phys. Rev. B*, 2015, **91**, 085207.
69 G. J. Snyder, A. H. Snyder, M. Wood, R. Gurunathan, B. H. Snyder and C. Niu, *Adv. Mater.*, 2020, **32**, e2001537.
70 S. D. Kang and G. J. Snyder, 2017, arXiv:1710.06896 [cond-mat.mtrl-sci].

